



1

2 **Supporting Information for**

3 **Spiking at the edge: Excitability at interfaces in reaction-diffusion systems**

4 **Colin Scheibner, Hillel Ori, Adam E. Cohen and Vincenzo Vitelli**

5 **Vincenzo Vitelli.**

6 **E-mail: vitelli@uchicago.edu**

7 **This PDF file includes:**

- 8 Supporting text
- 9 Figs. S1 to S7
- 10 Legends for Movies S1 to S2
- 11 SI References

12 **Other supporting materials for this manuscript include the following:**

- 13 Movies S1 to S2

Supporting Information Text

1. Population dynamics

In dimensionful units, the Lotka-Volterra model we consider takes the form (1):

$$\dot{P} = -aP + bN(P + g)R_p(P) \quad [S1]$$

$$\dot{N} = cNR_n(N) - dPN \quad [S2]$$

where P is the population of the predator, N is the population of the prey, and $a, b, c, d, g > 0$. Here, a is the dimensionful hopping rate at which the lumberjacks (predator) travel into the desert and perish; b sets the benefit to the lumberjacks of consuming a tree; c is the growth rate of the trees; and d sets the intensity of the predation. The parameter g is a regularization parameter that prevents the lumberjacks from going extinct. We will eventually be interested in the limit $g \rightarrow 0$. The function $R_n(N)$ is a nonlinearity that sets the carrying capacity K_n for the prey in absence of predators. We require that $R_n(0) = 1$ and that R_n only crosses zero at K_n . Likewise, $R_p(P)$ obeys $R_p(0) = 1$ and only crosses zero at K_p , the carrying capacity of the predators.

We nondimensionalize Eqs. (S1-S2) by introducing a time scale $t_0 = 1/bK_n$ and defining

$$p = \frac{P}{K_p} \quad n = \frac{N}{K_n} \quad [S3]$$

$$\gamma = \frac{g}{K_p} \quad \epsilon = at_0 \quad [S4]$$

$$k(p) = R_p(pK_p) \quad r_n(n) = R_n(nK_n) \quad [S5]$$

$$\tau = \frac{1}{t_0c} \quad \tilde{t} = t/t_0 \quad [S6]$$

$$q = \frac{1}{dK_pt_0} \quad [S7]$$

yielding the equations:

$$\dot{p} = -\epsilon p + n(p + \gamma)k(p) \quad [S8]$$

$$\dot{n} = \frac{n}{\tau} \left[r_n(n) - \frac{p}{q} \right] \quad [S9]$$

in which all quantities are dimensionless. For the phase portraits in Fig. 2a-c, we use the following piecewise linear functions for $r_n(n)$ and $k(p)$:

$$r_n(n) = 1 - n \quad [S10]$$

$$k(p) = \Theta(p_* - p) \left(\frac{p(n_* - 1)}{p_*} + 1 \right) + \Theta(p - p_*) \frac{n_*(p - 1)}{p_* - 1} \quad [S11]$$

where $p_* = 0.7$ and $n_* = 3$. We use $\epsilon = 0, 0.5$, and 4.0 for panels a, b, and c respectively. For all panels we use $\tau = 50$ and $q = 0.5$.

Next, we detail the passage to the continuum shown in Fig. 2e-g. Consider a compartment model with local populations p_i and n_i , where $-N \leq i \leq N$. Here, a positive index i corresponds to the forest, and a non-positive i corresponds to the desert. The dynamics are governed by

$$\dot{p}_i = \epsilon(p_{i+1} - p_{i-1} - 2p_i) + \begin{cases} -\alpha p_i & -N \leq i \leq 0 \\ n_i(p_i + \gamma)k(p_i) & 1 \leq i \leq N \end{cases} \quad [S12]$$

$$\dot{n}_i = \frac{n_i}{\tau} \left[r_n(n_i) - \frac{p_i}{q} \right] \quad [S13]$$

with boundary conditions $p_{-N-1} \equiv p_{-N}$ and $p_{N+1} \equiv p_N$. As in Eq. (1), the parameter ϵ in Eq. (S12) sets the hopping rate between sites. However, in Eq. (S12) we allow the desert to have an intrinsic strength α that is no longer necessarily infinite. One recovers Eqs. (1-2) by taking $N = 1$ and $\alpha \rightarrow \infty$, in which case $p_{-1} = p_0 = 0$ may be eliminated. Likewise, Fig. 2e, f, and g correspond to taking $\alpha \rightarrow \infty$ with $N = 2$, $N = 4$, and $N = 100$ respectively. See SI §5 for simulation details.

The continuum limit applies when $N, \epsilon \gg 1$ and the discrete index i is replaced by a continuous variable $x = id$, where d is the lattice spacing. If $\alpha \rightarrow \infty$, then $p(x < 0) = 0$, so the continuum equations take the form

$$\dot{p} = \nabla^2 p + n(p + \gamma)k(p) \quad [S14]$$

$$\dot{n} = \frac{n}{\tau} \left[r_n(n) - \frac{p}{q} \right] \quad [S15]$$

paired with the Dirichlet boundary $p(0) = 0$ and the no-flux boundary $\partial_x p|_\ell = 0$. Here, we have nondimensionalized the x -coordinate according to $x \rightarrow x/\sqrt{D}$ and $\ell = L/\sqrt{D}$. However, if α is finite, then one obtains an interfacial equation of the form:

$$\dot{p} = \nabla^2 p + \begin{cases} -\alpha p & x \in [-\ell, 0] \\ n(p + \gamma)k(p) & x \in [0, \ell] \end{cases} \quad [\text{S16}]$$

$$\dot{n} = \frac{n}{\tau} \left[r_n(n) - \frac{p}{q} \right] \quad [\text{S17}]$$

29 with no-flux boundaries at $x = \pm\ell$. We use Eq. (S17) with $\alpha = 1$ to produce the kymograph in Fig. 1b. See SI §5 for simulation
30 details.

To compute the phase diagram in Fig. 2h, notice that Eqs. (S14-S15) take the same form as Eqs. (14-15). Here, p is the fast variable, n is the slow variable, and the function \tilde{f} is given by $\tilde{f}(p) = (p + \gamma)k(p)$. The function n_∞ (which plays the role of B_∞) is determined by the functional form of r_n . For instance, consider the piecewise linear function

$$r_n(n) = \begin{cases} 1 - mn & n \in [0, \frac{1-q}{m}] \\ q & n \in [\frac{1-q}{m}, 1 - \frac{q}{m}] \\ m(1 - n) & n \in [1 - \frac{q}{m}, 1] \end{cases} \quad [\text{S18}]$$

31 If $m = 1$, then $r_n(n) = 1 - n$ and $n_\infty(p) = \max\{0, 1 - p/q\}$. If $m \rightarrow \infty$, then $n_\infty(p) = \Theta(q - p)$, where q plays the role of A_*
32 in Methods §B. The phase diagrams in Fig. 2d and Fig. 2h are analytically computed for $m \rightarrow \infty$. In the limit that $\gamma \rightarrow 0$, the
33 location of the local maximum of $X(q)$ approaches $q = 0$ and so the general phase diagram in Fig. 9a converges the one Fig. 2h.

2. Bioelectric interfaces

A. Conductance-based bioelectric model. The bioelectric dynamics we consider are described by conductance-based (i.e. Hodgkin-Huxley type) models. Our equations focus on the role of the sodium ion channels, potassium ion channels, and gap-junction coupling between cells. If the ion channels are homogeneously distributed throughout the tissue, the dynamics are governed by

$$C\dot{V} = G\nabla^2 V + g_K f_K(V) + h g_{Na} f_{Na}(V) \quad [S19]$$

$$\dot{h} = \frac{h_\infty(V) - h}{\tau} \quad [S20]$$

Here, $V(x, t)$ is the local membrane potential of the tissue, C is the capacitance of the cell membrane, $g_K f_K(V)$ and $h g_{Na} f_{Na}(V)$ are the currents through the potassium and sodium channels, respectively. The constants g_K and g_{Na} are known as open-state conductances, and they set the relative strengths of the potassium and sodium channels. The functions f_K and f_{Na} are nonlinearities that control the shape of the voltage-current relationship. The variable h is a gating variable that assumes values between 0 and 1, and τ is a time constant for its evolution towards a steady state value $h_\infty(V)$. Finally, voltage diffusion, modulated by the parameter G , arises due to gap-junction coupling.

To nondimensionalize the equations, let V_{ref} be a characteristic reference voltage, set $r = \frac{g_{Na}}{g_K}$ to be the relative strength of the sodium and potassium channels, and let $t_0 = \frac{V_{\text{ref}} C}{g_K}$ denote a characteristic time of the voltage dynamics. Next, let $D = G V_{\text{ref}} / g_K$ be the diffusion coefficient G/C times the characteristic time scale t_0 . Note that \sqrt{D} has dimensions of length. We nondimensionalize the equations according to

$$\tilde{h} = h r \quad [S21]$$

$$\tilde{t} = t / t_0 \quad [S22]$$

$$\tilde{\tau} = \tau / t_0 \quad [S23]$$

$$\tilde{V} = V / V_{\text{ref}} \quad [S24]$$

$$\tilde{x} = x / \sqrt{D} \quad [S25]$$

$$\tilde{f}_K(\tilde{V}) = f_K(\tilde{V} V_{\text{ref}}) \quad [S26]$$

$$\tilde{f}_{Na}(\tilde{V}) = f_{Na}(\tilde{V} V_{\text{ref}}) \quad [S27]$$

In the main text, we use dimensionless variables except for x , and hence D is also retained in Eqs. (5-6). In what follows, we will work in dimensionless quantities and omit the tildes.

As shown in Fig. 3c,f,i, we will require that $f_K(V)$ and $f_{Na}(V)$ each have exactly one zero crossing, at V_K and V_{Na} respectively, and that they are decreasing at this zero. Also, motivated by experimentally calibrated conductance models (2), we take the asymptotic value of the gating variable to be a step function: $h_\infty(V) = r \Theta(V_* - V)$, where V_* is the crossover of the step.

B. Dynamics of a single cell. Before considering a spatially extended system, we consider the dynamics of a single cell with both sodium and potassium channels, described by the ordinary differential equation

$$\dot{V} = f_K(V) + h f_{Na}(V) \quad [S28]$$

$$\dot{h} = \frac{h_\infty(V) - h}{\tau} \quad [S29]$$

The dynamics of a single cell can be understood in terms of the V and h nullclines. For example, in Fig. S1, the solid red line indicates h_∞ , which is the h -nullcline. The solid black line indicates the V -nullcline, given by

$$h_{\text{eq}}(V) = -\frac{f_K(V)}{f_{Na}(V)} \quad [S30]$$

As shown in Fig. S1 and Fig. 3d,g, the V_* - r phase diagram for single cell exhibits spiking if h_{eq} is an “N” shaped curve. However, if h_{eq} is monotonically increasing (e.g., Fig. 3j), then the V_* - r phase diagram for a single cell does not exhibit spiking.

C. Phase diagram for interfacial spiking. Here we derive the phase diagram for the bioelectric interface shown in Fig. 3. We will consider a 1D domain, $x \in [-\ell, \ell]$, with an interface at $x = 0$. We will be particularly interested in the following two limits: $\ell \rightarrow 0$, in which we will recover the single-cell phase diagrams in Fig. 3d,g,j; and $\ell \rightarrow \infty$, in which we obtain the interfacial phase diagrams in Fig. 3e,h,k. The governing equations are:

$$\dot{V} = \nabla^2 V + \begin{cases} f_K(V) & x \in [-\ell, 0] \\ h f_{Na}(V) & x \in (0, \ell] \end{cases} \quad [S31]$$

$$\dot{h} = \frac{h_\infty(V) - h}{\tau} \quad [S32]$$

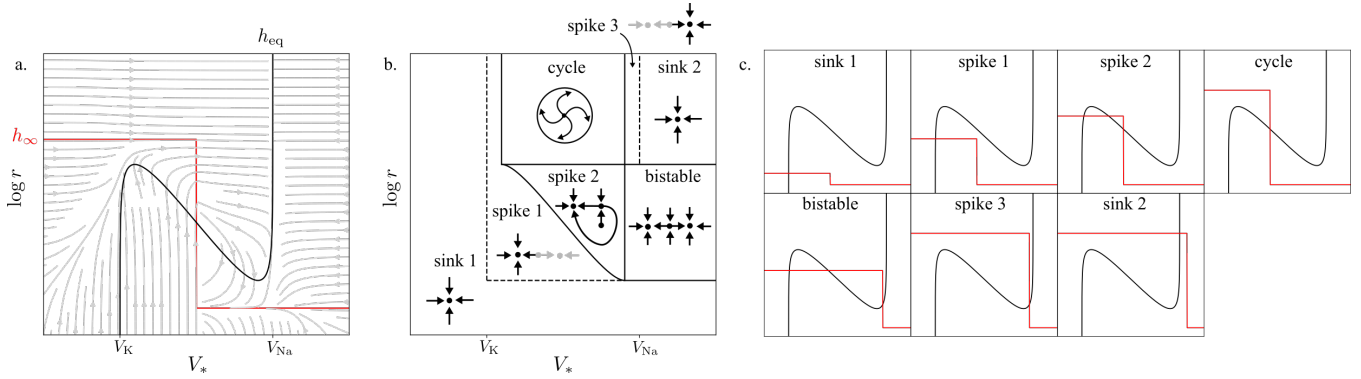


Fig. S1. A spiking phase diagram for a single bioelectric cell. **a.** A representative phase portrait for Eqs. (S28-S29). The fixed point (here unstable) appears at the intersection h_{eq} (black) and h_{∞} (red). **b.** An annotated phase diagram showing the fixed points, limit cycles, and heteroclinic orbits in each phase. The light grey points and arrows represent features that are only present in the $\tau \rightarrow \infty$ dynamics. **c.** The h_{eq} and h_{∞} curves for each phase in the phase diagram.

We will require that V and $\partial_x V$ be continuous and that $\partial_x V|_{\pm\ell} = 0$. For brevity, we will write:

$$f(V, h, x) = f_K(V)\Theta(-x) + hf_{Na}(V)\Theta(x) \quad [S33]$$

Following the general approach from Methods §B, we first solve for the fixed points of Eqs. (S31-S32), which we refer to as stationary solutions. Setting the left-hand side of Eqs. (S31-S32) to zero amounts to solving the equation:

$$0 = \nabla^2 V + f(V, h_{\infty}(V), x) \quad [S34]$$

which can be cast as a Hamiltonian system

$$\partial_x V = P \quad [S35]$$

$$\partial_x P = -f(V, h_{\infty}(V), x) \quad [S36]$$

with boundary conditions $P|_{\pm\ell} = 0$. As shown in Fig. S2, Eqs. (S35-S36) may be solved graphically. First, construct the curve $P_K(V; \ell)$ by taking the line $P = 0$ and advecting it forward a distance ℓ according to the $x < 0$ flow, as shown in Fig. S2a. Second, construct the curve $P_{Na}(V; -\ell)$ by advecting the line $P = 0$ backwards a distance ℓ according to the $x > 0$ flow, as shown in Fig. S2b. The intersections $P_K(V; \ell) = P_{Na}(V; -\ell)$ correspond to stationary solutions. We will focus on two limits:

First, we consider $\ell \rightarrow 0$. In this limit, we expect to recover the dynamics of a single cell, since V is effectively forced to be constant across the domain $[-\ell, \ell]$. Indeed, for small ℓ , one obtains

$$P_K(V; \ell) = -\ell f_K(V) + \mathcal{O}(\ell^2) \quad [S37]$$

$$P_{Na}(V; -\ell) = \ell h_{\infty}(V) f_{Na}(V) + \mathcal{O}(\ell^2) \quad [S38]$$

Equating $P_K(V; \ell) = P_{Na}(V; -\ell)$ yields

$$h_{eq}(V) = h_{\infty}(V) \quad [S39]$$

which is the fixed point equation for a single cell described by Eqs. (S28-S29).

Second, we consider $\ell \rightarrow \infty$. In this limit, $P_K(V; \ell)$ and $P_{Na}(V; -\ell)$ approach the separatrices of the Hamiltonian flow, as shown in Fig. S2a-b. These separatrices are given explicitly by:

$$P_K(V) = \sqrt{-2 \int_{V_K}^V f_K(V') dV'} \quad [S40]$$

$$P_{Na}(V) = \sqrt{2 \int_V^{V_{Na}} h_{\infty}(V') f_{Na}(V') dV'} \quad [S41]$$

Since f_K and f_{Na} only have one zero crossing each, the separatrices are monotonic and they will only intersect once. Hence, in the limit $\ell \rightarrow \infty$, the stationary solution $V_0(x)$ is unique. Until this point, we have only required that $h_{\infty}(V)$ be non-negative on the interval $[V_K, V_{Na}]$. For $h_{\infty}(V) = r \Theta(V_* - V)$, the solution $V_0(x)$ is the curve that matches between the left- and right-hand side while reaching $\partial_x V = 0$ at the voltage V_* , as shown in Fig. S2c. We will let x_* denote the solution to the equation $V_0(x) = V_*$. We note that the intersection construction in Fig. S2a-b is equivalent to the hill picture provided in Fig. 4a in which V is the position of the ball and P is its momentum.

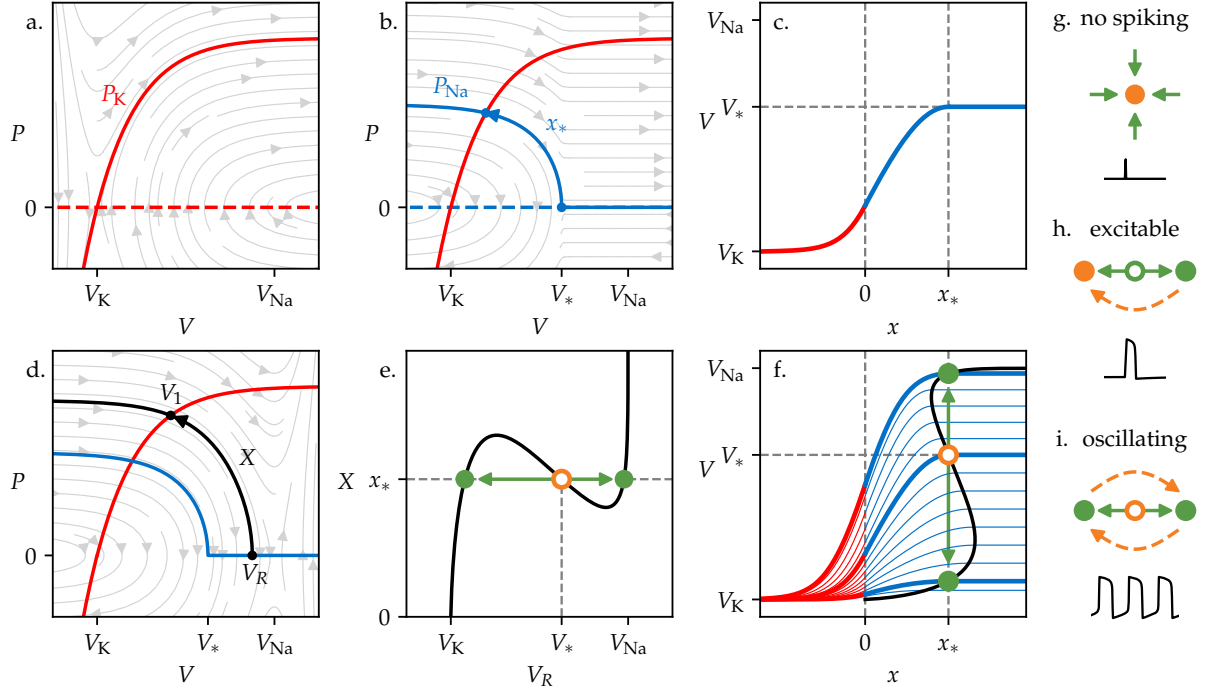


Fig. S2. Bifurcation analysis of interfacial spiking. **a.** The Hamiltonian flow in Eqs. (S35-S36) for $x < 0$ is depicted. The separatrix P_K (solid blue line) results from an advection of $P = 0$ (dashed blue line) through a distance $\ell \rightarrow \infty$. **b.** Similarly, the Hamiltonian flow in Eqs. (S35-S36) for $x > 0$ is depicted. The separatrix P_{Na} (solid red line) results from an advection of $P = 0$ (dashed red line) through a distance $\ell \rightarrow -\infty$. Solving for the separatrices amounts to solving the differential equations on either side of the interface in Eqs. (5-6). Finding the intersection of P_{Na} and P_K amounts to enforcing the continuity requirements for V and $\partial_x V$ at $x = 0$. **c.** In real space, composing the separatrices yields the stationary solution $V_0(x)$. The curve $V_0(x)$ matches the $x < 0$ and $x > 0$ solutions subject to the requirement that the right solution obtains a slope of zero at $V = V_*$. **d.** The curve $P_{Na}(V, V_R)$ is shown in black. V_R is the V coordinate of the intersection with $P = 0$, and V_1 marks the intersection with P_K . The function $X(V_R)$ represents the x distance transversal in real space between the voltages V_R and $V_1(V_R)$. **e.** The function X is plotted as a function of V_R . The number of solutions to the equation $X(V_R) = x_*$ varies from 1 to 3 depending on x_* . **f.** One can visualize the function $X(V_R)$ (black curve) by plotting a range of trial solutions with different slopes at their interface. The function $X(V_R)$ corresponds to the x value at which each curve first attains its maximum. The thick lines correspond to the critical points of Φ . **g.** If x_* intersects X once, then the system does not exhibit spikes. **h.** If x_* intersects X three times with V_* corresponding to an increasing branch, then the system exhibits excitability. **i.** If V_* lies on the decreasing branch of X , then the system exhibits oscillations. In (e-i), the circles represent critical points of the functional Φ in Eqs. (S42). The orange circle represents $V_0(x)$, the stationary solution of Eqs. (S31-S32). Solid arrows represent fast heteroclinic orbits, and the dashed arrows represent slow dynamics in Eqs. (S31-S32). Open circles are unstable critical points, while solid circles are stable critical points of Φ .

Having found the stationary solution $V_0(x)$, we examine the fast dynamics with h frozen to $h_\infty(V_0(x))$. The fast dynamics are governed by:

$$\dot{V} = \nabla^2 V + F(V, x) = -\frac{\delta \Phi}{\delta V} \quad [\text{S42}]$$

where $F(V, x) = f(V, h_\infty(V_0(x)), x)$. As in Methods §B, we seek to find the critical points of Φ , i.e. solve Eq. (S42) with $\dot{V} = 0$. This amounts to solving the system:

$$\partial_x V = P \quad [\text{S43}]$$

$$\partial_x P = -F(V, x) \quad [\text{S44}]$$

with boundary conditions $P(\pm\ell) = 0$.

In the limit $\ell \rightarrow \infty$ we construct the solutions to Eqs. (S43-S44) as follows:

1. First define

$$P_{Na}(V, V_R) = \sqrt{2r \int_V^{V_R} f_{Na}(V') dV'} \quad [\text{S45}]$$

2. Second, define $V_1(V_R)$ to be the point of intersection between the left separatrix and the right solution curves, i.e. $P_K(V_1) = P_{Na}(V_1, V_R)$, as shown in Fig. S2d.

3. Thirdly, compute

$$X(V_R) = \int_{V_1(V_R)}^{V_R} \frac{1}{P_{Na}(V, V_R)} dV \quad [\text{S46}]$$

which is the distance in real space between the locations where the voltage crosses V_1 and V_R .

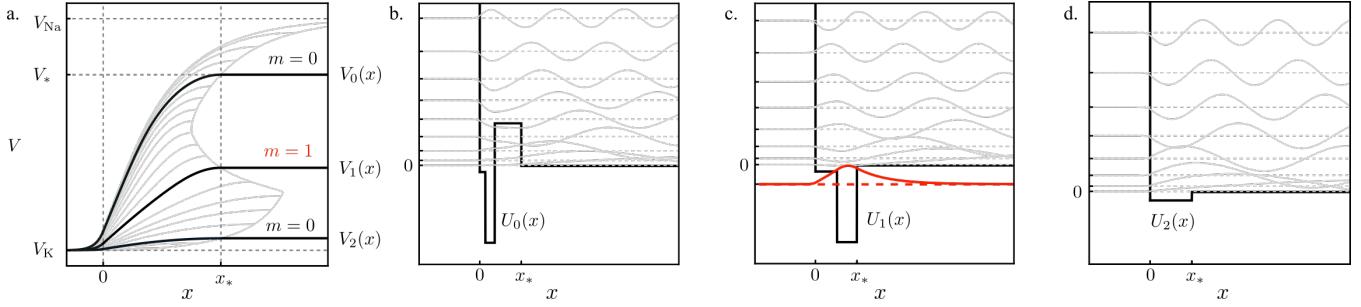


Fig. S3. Linearized dynamics and interface confinement. **a.** An example of three solutions to Eq. (S42) (black lines), which constitute critical points of the functional Φ . The light gray curves represent trial solutions that do not meet the boundary conditions. **b–d.** The linearized dynamics about each critical point p is governed by a Schrödinger equation with an effective potential U_p . Each effective potential features a well near the interface. The unstable dimension, m , of each critical point corresponds to the number of negative energy states of the Hamiltonian. Because the negative energy states must be bound states, the unstable modes that drive the spiking feature a spatial profile that is localized near the interface. The sole negative energy state in (c) is highlighted in red.

4. Finally, as illustrated in Fig. S2e, critical points [i.e. solutions of Eq. (S43–S44)] correspond to solutions of the equation $X(V_R) = x_*$.

As illustrated in Fig. S2f, the construction of $X(V)$ can be visualized in real space: for a range of trial solutions with different slopes at the interface, the points at which each curve first achieves $\partial_x V = 0$ forms the graph $(X(V), V)$. Critical points of Φ are the curves for which $X(V) = x_*$. In SI §6, we analyze a special case in which f_K and f_{Na} are piecewise linear, allowing $X(V)$ and $V_0(x)$ to be computed analytically in terms of trigonometric functions.

We note that the precise shape of $X(V)$ depends on the functions f_K and f_{Na} and the parameter r . Nevertheless, the hypotheses $f_K(V) < 0$ and $f_{Na}(V) > 0$ for $V \in (V_K, V_{Na})$ imply that $X(V_K) = 0$ and $X(V_{Na}) = \infty$. If we specialize to the situation in which $X(V)$ is “N” shaped, we can use the same stability arguments as in Methods §B to obtain the spiking phase diagrams shown in Fig. 3e,h,k: If $X(V_*)$ has degeneracy 1, then the system cannot spike (see Fig. S2g). If $X(V_*)$ has degeneracy 3, then the system can spike. If V_* lies on an increasing branch of X , then $V_0(x)$ is stable and the system is excitable (see Fig. S2h). If V_* lies on the decreasing branch of X , then $V_0(x)$ is unstable and the system exhibits a oscillations (see Fig. S2i).

D. Limits: $r \rightarrow 0, r \rightarrow \infty$. If the potassium channels are much stronger than the sodium channels, then one expects that the interface will behave as a Dirichlet boundary with $V(0) = V_K$. This can be shown mathematically by taking the limit $r \rightarrow 0$. From the definition of $V_1(V_R)$, namely $P_K(V_1) = P_{Na}(V_1, V_R)$, we obtain the relationship

$$\int_{V_K}^{V_1} f_K(V) dV + r \int_{V_1}^{V_R} f_{Na}(V) dV = 0 \quad [\text{S47}]$$

From Eq. (S47) one sees that $V_1 \rightarrow V_K$ as $r \rightarrow 0$. In this limit, the expression for $X(V_R)$ [Eq. (S47)] becomes:

$$X_{\text{low}}(V_R) = \frac{1}{\sqrt{2r}} \int_{V_K}^{V_R} \frac{1}{\sqrt{U_{Na}(V) - U_{Na}(V_R)}} dV \quad [\text{S48}]$$

where U_{Na} is an antiderivative of f_{Na} . Notice that Eq. (S48) has the same functional form as Eq. (20) in the Methods. Crucially, r only appears as a multiplicative prefactor of $X(V_R)$, implying that the phase boundaries become independent of r as $r \rightarrow 0$. Furthermore, the form of $X(V)$ and hence the phase diagram at low r only depends on the functional form f_{Na} and on the zero crossing V_K , but not on the detailed functional form of f_K .

Similarly, in the limit that $r \rightarrow \infty$, we may write $V_1 = V_R - \delta(r)$ where $\delta(r) \ll 1$. From Eq. (S47), one concludes

$$\delta = \frac{U_K(V_R) - U_K(V_K)}{r f_{Na}(V_R)} + \mathcal{O}(1/r^2) \quad [\text{S49}]$$

where U_K is an antiderivative of f_K . Then the expression for $X(V_R)$ [Eq. (S47)] becomes

$$X_{\text{high}}(V_R) = \sqrt{\frac{2\delta}{f_{Na}(V_R)}} \quad [\text{S50}]$$

$$= \frac{\sqrt{2}}{r} \frac{\sqrt{U_K(V_K) - U_K(V_R)}}{f_{Na}(V_R)} \quad [\text{S51}]$$

Once again, r appears a multiplicative prefactor, implying that the phase boundaries become vertical in the V_* - r plane. Notice that Eq. (S51) depends on the functional form of both f_{Na} and f_K , implying that $X_{\text{high}}(V_R)$ and $X_{\text{low}}(V_R)$ can be tailored independently of each other.

E. Shape of unstable modes. Here we discuss why the spatial profile of the edge spike is often localized near the interface or boundary (see Fig. 1a-b for example). As illustrated in Fig. S2f, the critical points of Φ (i.e. the curves intersecting green circles) are monotonically increasing. However, when τ is finite, the voltage profile $V(x, t)$ approaches the critical points, but does not completely reach them because the voltage takes a non-negligible amount of time to diffuse out to the boundaries (especially for large systems). Instead, the spatial extent of the spike is better approximated by the shape of the unstable mode associated with the unstable critical point. Given a critical point p , with spatial profile $V_p(x)$, the linearized dynamics obey:

$$\partial_t \delta V = -H \delta V \quad [\text{S52}]$$

where $\delta V(x) = V(x) - V_p(x)$ and

$$H(x) = -\nabla^2 + U(x) \quad [\text{S53}]$$

with $U(x) = -\frac{\partial F}{\partial V}|_{V_p(x)}$. Notice that Eq. (S52) is a 1D Schrödinger equation with potential $U(x)$. As an illustration, Fig. S3a show the voltage profile for a bioelectric interface for which Φ has three critical points, $V_0(x)$, $V_1(x)$, and $V_2(x)$. Figure S3b-d shows the effective potential for each of these three critical points. (In this example, f_K and f_{Na} are chosen to be piecewise linear, and hence each $U_p(x)$ is a square well). Negative eigenvalues of H correspond to unstable modes. Since we require $\partial_x V|_{\pm\infty} = 0$ and $f_K(V)$ and $f_{Na}(V)$ are both decreasing at their zero crossings, it follows that $U(x \rightarrow \pm\infty)$ approaches non-negative constants $C_1 = -h_\infty(V_{Na})\partial_V f_V$ and $C_2 = -\partial_V f_K$. Therefore negative energy states, and hence the unstable modes, correspond to bound states of $U(x)$. Naturally, these bound states are confined to the well formed by $U(x)$, which coincides with the region in which $V_p(x)$ interpolates between its two asymptotic values. Examples of the linear spectrum for each critical point are shown Fig. S3b-d. In accordance with the stability of each critical point, only panel c has a negative energy state, which is highlighted in red.

F. Example ion channels. Here we provide the expression for the ion channels used in Fig. 3. For panels (c-e), we use:

$$f_K(V) = \frac{(V_K - V)e^{-2.5(V-V_K)}}{N_1} \quad [\text{S54}]$$

$$f_{Na}(V) = \frac{(V_{Na} - V)e^{2.5(V-V_{Na})}}{N_2} \quad [\text{S55}]$$

For panels (f-h), we use:

$$f_K(V) = \frac{-e^{-(V-V_K)} + e^{-2(V-V_K)}}{N_3} \quad [\text{S56}]$$

$$f_{Na}(V) = \frac{e^{(V-V_{Na})} - e^{2(V-V_{Na})}}{N_4} \quad [\text{S57}]$$

For panels (i-k), we use:

$$f_K(V) = \frac{0.3(1 - e^{(V-V_K)})}{N_5} \quad [\text{S58}]$$

$$f_{Na}(V) = \frac{e^{2.5V}(V_{Na} - V)}{N_6} \quad [\text{S59}]$$

with $V_K = -1$ and $V_{Na} = 1$. The normalization constants N_1, \dots, N_6 are chosen such that the local minimum or maximum of each ion channel is normalized to -1 and 1 , respectively.

95 3. Oscillating chemical reactions

The chemical dynamics we study involve two chemical reservoirs undergoing distinct chemical reactions. In the rightmost chamber, we consider a prototypical chemical reaction network known as the Oregonator (3). The Oregonator can be summarized by 5 elementary reactions



96 with rate constants k_i . Here R is a reactant, P is the product, A , B , and C are catalysts, and m_1 is a stoichiometric coefficient. The Oregonator was originally proposed as a minimal model for the Belousov-Zhabotinsky reaction (4). In this context, the variables can be roughly interpreted as: $R = \text{BrO}_3^-$, $P = \text{HOBr}$, $A = \text{Br}^-$, $B = \text{Ce}^{4+}$, and $C = \text{HBrO}_2$, and suitable rate constants can be determined from experiments. See Ref. (4) for a detailed introduction.

In the right chamber, we assume that the reactant R is abundant, so its concentration can be treated as constant. Moreover, the product P is assumed to exit the reaction and not affect the subsequent dynamics. Hence, we need only consider the kinetic equations for the intermediates A , B , and C :

$$\dot{A} = -k_1 R A - k_2 C A + m_1 k_5 B \quad [S60]$$

$$\dot{B} = 2k_3 R C - k_5 B \quad [S61]$$

$$\dot{C} = k_1 R A - k_2 C A + k_3 R C - k_4 C^2 \quad [S62]$$

Here, A denotes the concentration of component A , etc. We nondimensionalize the kinetic equations by introducing a time scale $t_0 = \frac{k_4}{k_3 k_2 R}$ and defining

$$a = \frac{k_2}{R k_3} A \quad b = \frac{k_4 k_5}{2(R k_3)^2} B \quad [S63]$$

$$c = \frac{k_4}{R k_3} C \quad \tilde{t} = t/t_0 \quad [S64]$$

resulting in

$$\dot{a} = 2m_1 b - a(c + m_2) \quad [S65]$$

$$\dot{b} = \frac{c - b}{\tau} \quad [S66]$$

$$\epsilon \dot{c} = a(m_2 - c) + c(1 - c) \quad [S67]$$

with the parameters

$$\epsilon = \frac{k_2}{k_4} \quad \tau = \frac{k_2 k_3 R}{k_4 k_5} \quad m_2 = \frac{k_1 k_4}{k_2 k_3} \quad [S68]$$

We are interested in the regime $\epsilon \ll 1$ and $\tau \gg 1$. With $\epsilon \ll 1$, we may integrate out Eq. (S67) and define

$$c(a) = b_\infty(a) \equiv \frac{1}{2} \left[(1 - a) + \sqrt{(1 - a)^2 + 4m_2 a} \right] \quad [S69]$$

Thus the dynamics become

$$\dot{a} = 2m_1 b - a(b_\infty(a) + m_2) \quad [S70]$$

$$\dot{b} = \frac{b_\infty(a) - b}{\tau} \quad [S71]$$

The b -nullcline is given by $b = b_\infty$ and the a -nullcline $\dot{a} = 0$ is given by

$$b = b_{\text{eq}}(a) \equiv \frac{a(b_\infty(a) + m_2)}{2m_1} \quad [S72]$$

100 Depending on the values of m_1 and m_2 , Eqs. (S70-S71) can exhibit no-spiking, excitable, and oscillating phases. Our interest
101 is in the regime in which m_1 is sufficiently large to create local excitability, as shown in Fig. S4.

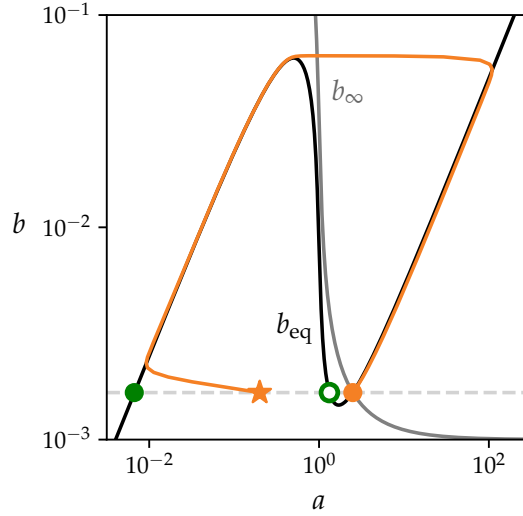


Fig. S4. A phase portrait of an excitable chemical reaction. A phase portrait for Eqs. (S70-S71) with $m_1 = 2$, $m_2 = 10^{-3}$, $\tau = 10^4$. The black curve is $b_{\text{eq}}(a)$ [Eq. (S72)] and the grey curve is $b_{\infty}(a)$ [Eq. (S69)]. The solid and filled green circles represent critical points of the fast dynamics (cf. Fig. 6). The orange curve is an example trajectory starting at the star and ending at the orange solid circle and exhibiting a spike. The same parameters are used to integrate Eqs. (S76-S77) in Fig. 1c. Notably, the interface exhibits oscillation, rather than excitability, due to the presence of diffusion.

For a spatially extended system, Eqs. (S67-S66) become

$$\dot{a} = \nabla^2 a + 2m_1 b - a(c + m_2) \quad [\text{S73}]$$

$$\dot{b} = \beta \nabla^2 b + \frac{c - b}{\tau} \quad [\text{S74}]$$

$$\varepsilon \dot{c} = \alpha \nabla^2 c + a(m_2 - c) + c(1 - c) \quad [\text{S75}]$$

In Eqs. (S73-S74), we nondimensionalize length using $x \rightarrow x/\sqrt{D}$ where $D = D_A t_0$ and D_A is the diffusion constant for species A. In Eq. (S75) and Eq. (S74), $\alpha = \varepsilon \frac{D_C}{D_A}$ and $\beta = \frac{D_B}{D_A}$, where D_C and D_B are the diffusion constants for C and B, respectively. Since $\varepsilon \ll 1$, we have $\alpha \ll 1$ and therefore c can be locally integrated out using Eq. (S69).

In the leftmost chamber, we assume that the catalyst A is rapidly converted into a product and exits the reaction:



When the species A is allowed to diffuse across the interface, the governing equations take the form:

$$\dot{a} = \nabla^2 a + \begin{cases} -a & x \in [-\ell, 0] \\ 2m_1 b - a[b_{\infty}(a) + m_2] & x \in [0, \ell] \end{cases} \quad [\text{S76}]$$

$$\dot{b} = \frac{b_{\infty}(a) - b}{\tau} \quad [\text{S77}]$$

For Fig. 1c, we choose $m_1 = 2$ and $m_2 = 10^{-3}$. In this case, the $x > 0$ reservoir displays excitability (see the phase portrait in Fig. S4), and the $x < 0$ reservoir exhibits no spiking. Crucially, however, when the catalyst A is allowed to diffuse, the full interfacial system exhibits oscillations.

4. Design of the binary half adder

Here we comment on the design of the binary half adder in Fig. 5c-d. Each input channel encodes a Boolean value: *true* corresponds to the presence of a wave train, and *false* corresponds to the absence of a wave train. Within this paradigm, a self-contained logic gate receives input wave trains, subjects them to nonlinear interference, and produces output wave trains. Figure S5 shows examples of canonical OR, AND, NOT, and XOR logic gates. In each of these diagrams, a solid line indicates an interface of length $n\lambda$ and a dashed line indicates an interface length $(n + 1/2)\lambda$, where n is an integer, and $\lambda = Tc$, where T is the period of the input pulses and c is the wave velocity along the interface. Each of these logic gates is constructed using only two materials, which implies that each junction must comprise at least four interfaces. The device shown in Fig. 5c-d is known as a binary half adder, which takes the sum of two binary numbers. As shown in Fig. S6, the binary half adder can be constructed out of XOR and AND gates. In order to embed the logic gates in the 2D plane, an additional trivial gate $\text{CROSS}(x, y) = (x, y)$ must be implemented that allows two pulses to cross each other without performing a computation. To prevent undesired back scatter at interference junctions, a needle geometry shown in Fig. 5a-b is used.

In order for the gates in Fig. S5 to be composable, the phase of the output wave train must be independent of the choice of logically equivalent inputs. For example $\text{XOR}(T, F) = T$ and $\text{XOR}(F, T) = T$, so both inputs (T, F) and (F, T) must produce an output wave train with the same phase. However, if the output of the logic gate is the final output for the device, then the phase will not be read so certain logic gates, such as XOR, can be simplified. For example, in the binary half adder the XOR logic gate is simplified to XOR^* , as shown in Fig. S6.

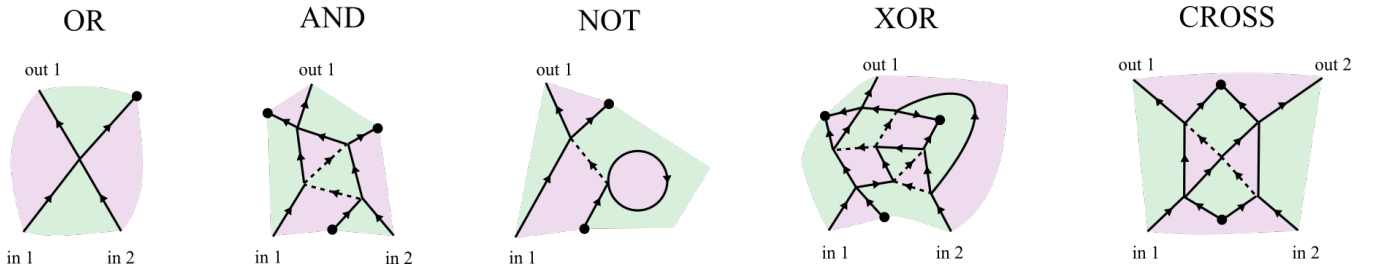


Fig. S5. Examples of OR, AND, NOT, XOR, and CROSS logic gates. The black lines represent interfaces between distinct materials (purple and green). Solid lines fit an integer number of wavelengths, while dashed lines fit a half integer number of wavelengths. The black circles represent termination points.

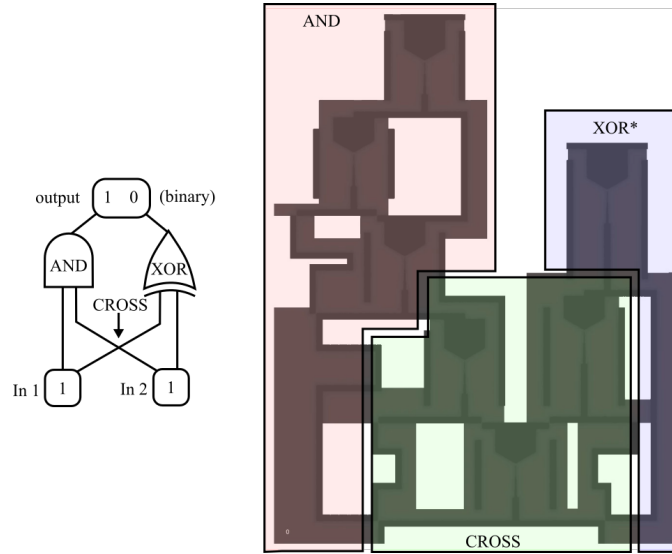


Fig. S6. Decomposition of binary half adder. A binary half adder can be decomposed into and AND gate and an XOR gates. Since the XOR gate generates an output of the system, it can be simplified to the XOR^* gate.

5. Numerics

Here we provide the details for the numerical simulations presented in main text.

Figure 1b. We integrate

$$\dot{p} = \nabla^2 p + \begin{cases} -p & x \in [-\ell, 0] \\ n p k(p) & x \in (0, \ell] \end{cases} \quad [\text{S78}]$$

$$\dot{n} = \frac{n}{\tau} \left[1 - n - \frac{p}{q} \right] \quad [\text{S79}]$$

with no-flux boundary conditions at $x = \pm\ell$. The parameters used are $\tau = 100$, $q = 0.5$, $\ell = 100$. The function $k(p)$ is given by Eq. (S11) with $p_* = 0.7$ and $n_* = 3$. An initial condition

$$p(x, 0) = 0.5(\tanh(x/10) + 1.1) \quad [\text{S80}]$$

$$n(x, 0) = 0.25(\tanh(-x/10) + 1.1) \quad [\text{S81}]$$

is used and a transient is allowed to pass prior to the time interval shown in Fig. 1b. The equations are discretized on a 1D lattice and integrated in Python using `scipy.integrate.solve_ivp`.

Figure 1c. We integrate Eqs. (M91-M92) with parameters $\ell = 100$, $\tau = 500$, $m_1 = 2.0$ and $m_2 = 0.001$. Our initial conditions are $a(x, 0) = b(x, 0) = 0.1$. An initial transient is allowed to pass prior to the time interval shown in Fig. 1c. The equations are discretized on a 1D lattice and integrated in Python using `scipy.integrate.solve_ivp`.

Figure 2e-g. The equations integrated are

$$\dot{p}_i = \epsilon(p_{i-1} + p_{i+1} - 2p_i) + n_i p_i k(p_i) \quad [\text{S82}]$$

$$\dot{n}_i = \frac{n_i}{\tau} \left(1 - n_i - \frac{p_i}{q} \right) \quad [\text{S83}]$$

for $i = 1, \dots, N$. Here $p_0 = 0$ represents the desert and setting $p_{N+1} \equiv p_N$ implements a no-flux boundary condition. The parameters used are $\epsilon = 4$, $q = 0.5$, $\tau = 20$. The function $k(p)$ is given by Eq. (S11) with $p_* = 0.7$ and $n_* = 3$. The initial conditions are given by $p_i = n_i = 0.6$. The equations are integrated in Python using `scipy.integrate.solve_ivp`.

Figure 4g-i. We integrate the equations

$$\dot{V} = \nabla^2 V + \begin{cases} f_K(V) & x \in [-\ell, 0] \\ h f_{Na}(V) & x \in (0, \ell] \end{cases} \quad [\text{S84}]$$

$$\dot{h} = \frac{r\Theta(V_* - V) - h}{\tau} \quad [\text{S85}]$$

with

$$f_K(V) = -V \quad [\text{S86}]$$

$$f_{Na}(V) = \begin{cases} 0 & V < V_a \\ \frac{b(V-V_a)}{V_b-V_a} & V_a \leq V < V_b \\ \frac{(1-b)(V-V_b)}{W_{Na}-V_b} + b & V_b \leq V < W_{Na} \\ \frac{V-V_{Na}}{W_{Na}-V_{Na}} & V \geq W_{Na} \end{cases} \quad [\text{S87}]$$

In all three kymographs, we use $V_a = -0.1$, $V_b = 0.25$, $W_{Na} = 0.5$, $b = 0.1$, $V_{Na} = 1$, $r = 0.1$, $\ell = 100$, and $\tau = 1000$. For panels g, h, and i, we set $V_* = -0.1$, $V_* = 0.2$, $V_* = 0.3$, respectively. For panel g, the initial conditions are given by $V(x, 0) = 0.3$, $h(x, 0) = 0.0$. For panel h, we first initialize the voltage profile to $V(x) = 0.1(\tanh(x/10) + 1.1)$. We then perform a relaxation according to

$$\dot{V} = \nabla^2 V + \begin{cases} f_K(V) & x \in [-\ell, 0] \\ r\Theta(V_* - V)f_{Na}(V) & x \in [0, \ell] \end{cases} \quad [\text{S88}]$$

$$h = r\Theta(V_* - V) \quad [\text{S89}]$$

to obtain stationary profiles $(V_0(x), h_0(x))$. Finally, we integrate Eqs. (S84-S85) using the initial conditions $V(x, 0) = V_0(x) + 1.1$ and $h(x, 0) = h_0(x)$. For panel i, the initial conditions are given by:

$$V(x, 0) = 0.1(\tanh(x/10) + 1.1) \quad [\text{S90}]$$

$$h(x, 0) = 0.5 \quad [\text{S91}]$$

135 For all panels, the equations are discretized onto a 1D lattice and integrated in Python using `scipy.integrate.solve_ivp`.

Figure 5. We integrate the equations:

$$\dot{V} = \nabla^2 V + s(x, y, t) + \begin{cases} f_K(V) & (x, y) \in \text{Region 1} \\ hf_{Na}(V) & (x, y) \in \text{Region 2} \end{cases} \quad [\text{S92}]$$

$$\dot{h} = \frac{r\Theta(V_* - V) - h}{\tau} \quad [\text{S93}]$$

where f_K and f_{Na} are given by Eqs. (S86 -S87) with $V_a = -0.1$, $V_b = 0.25$, $W_{Na} = 0.5$, $b = 0.1$, $V_{Na} = 1$, $r = 0.1$, $V_* = 0.15$, and $\tau = 300$. The wave trains are generated by repeated Gaussian pulses

$$s(x, y, t) = \sum_{\alpha} A_{\alpha}(t) \exp\left\{\frac{(x - x_{\alpha})^2 - (y - y_{\alpha})^2}{400}\right\} \quad [\text{S94}]$$

where (x_{α}, y_{α}) are the points at which the pulses are initialized. Here, the amplitude is a periodic square wave:

$$A_{\alpha}(t) = \sum_{n \in \mathbb{Z}} \Theta(1 - t - nT - D_{\alpha}) - \Theta(t - nT) \quad [\text{S95}]$$

where $T = 2810$ is the period and D_{α} is a phase shift (only used to produce the interfering wave trains in Fig. 5b). The Laplacian is discretized onto a triangular mesh. Initial conditions are obtained by initializing $V(x, y, 0) = 0.16$ then performing a relaxation

$$\dot{V} = \nabla^2 V + \begin{cases} f_K(V) & (x, y) \in \text{Region 1} \\ r\Theta(V_* - V)f_{Na}(V) & (x, y) \in \text{Region 2} \end{cases} \quad [\text{S96}]$$

$$h = r\Theta(V_* - V) \quad [\text{S97}]$$

136 over a time interval $t \in [0, 400]$. The full dynamics, Eqs. (S92-S93), were then integrated over a time interval $t \in [0, 40000]$.
 137 Integration is performed in Python using the `scipy.integrate.solve_ivp` function.

138 6. Explicitly solvable bioelectric interface model

We now present an example of Eqs. (S31-S32) for which the stationary solutions and critical points can be computed explicitly. We note that explicit solutions are readily obtained whenever one can solve

$$\nabla^2 V = -f_K(V) \quad [\text{S98}]$$

$$\nabla^2 V = -rf_{Na}(V) \quad [\text{S99}]$$

analytically for arbitrary initial conditions. One example is to take f_K and f_{Na} to be piecewise linear in V , as shown in Fig. S7. Namely, we take:

$$f_K(V) = -mV \quad [\text{S100}]$$

$$f_{Na}(V) = \frac{b(V - V_a)}{V_b - V_a} \Theta_{[V_a, V_b]}(V) + \left(\frac{1-b}{W_{Na} - V_b} (V - V_b) + b \right) \Theta_{[V_b, W_{Na}]}(V) + \frac{V - V_{Na}}{W_{Na} - V_{Na}} \Theta_{[W_{Na}, V_{Na}]}(V) \quad [\text{S101}]$$

139 where for a given interval I , $\Theta_I(V) = 1$ if $V \in I$ and $\Theta_I(V) = 0$ if $V \notin I$. We will use the shorthand $\Theta_1 = \Theta_{[V_a, V_b]}$,
140 $\Theta_2 = \Theta_{[V_b, W_{Na}]}$, and $\Theta_3 = \Theta_{[W_{Na}, V_{Na}]}$. We require that $V_a < 0 < V_b < W_{Na} < V_{Na}$.

Given the form of Eq. (S100), the solution to Eq. (S98) is given by:

$$V(x) = V(0)e^{\sqrt{m}x} \quad [\text{S102}]$$

where we have enforced that $\partial_x V|_{-\infty} = 0$. Hence, the left separatrix is given by $P_K(V) = \sqrt{m}V$. The solution to Eq. (S99) is slightly more subtle. Since f_{Na} is piecewise linear in V , it will be the more convenient to solve for the inverse $x(V)$. Given the initial conditions $V(0) = V_I$ and $\partial_x V|_0 = P_I$, one obtains

$$x(V; V_I, P_I) = \int_{V_I}^V \frac{1}{P(V', V_I, P_I)} dV' \quad [\text{S103}]$$

where

$$P(V; V_I, P_I) = \sqrt{2r[F_{Na}(V_I) - F_{Na}(V)] + P_I^2} \quad [\text{S104}]$$

and F_{Na} is an antiderivative of f_{Na} . Since f_{Na} is piecewise linear, the antiderivative is straightforward to compute:

$$F_{Na}(V) = \frac{1}{2} \sum_i [A_i(V - B_i)^2 + C_i] \Theta_i(V) \quad [\text{S105}]$$

where

$$A_1 = \frac{b}{V_b - V_a} \quad B_1 = V_a \quad C_1 = 0 \quad [\text{S106}]$$

$$A_2 = \frac{1-b}{W_{Na} - V_b} \quad B_2 = \frac{bW_{Na} - V_b}{b-1} \quad C_2 = \frac{b(V_a - bV_a - V_b + bW_{Na})}{b-1} \quad [\text{S107}]$$

$$A_3 = \frac{1}{W_{Na} - V_{Na}} \quad B_3 = V_{Na} \quad C_3 = V_{Na} - V_b + b(W_{Na} - V_a) \quad [\text{S108}]$$

Therefore, we have:

$$P(V; V_I, P_I) = \sum_i \sqrt{D_i - rA_i(V - B_i)^2} \Theta_i(V) \quad [\text{S109}]$$

where

$$D_i = r[A_1(V_I - b_1)^2 + C_1 - C_i] + P_I \quad [\text{S110}]$$

In Eq. (S110) and onwards, we assume for simplicity that $V_I \in [V_a, V_b]$. Next, we recall the following antiderivative

$$\int \frac{1}{\sqrt{D - rA(V - B)^2}} dV = \frac{1}{\sqrt{rA}} \operatorname{atan} \left[\sqrt{\frac{rA}{D - rA(V - B)^2}} (V - B) \right] \quad [\text{S111}]$$

Thus we obtain the solution

$$x(V; V_I, P_I) = \sum_i X_i(V; V_I, P_I) \Theta_i(V) \quad [\text{S112}]$$

where

$$X_1(V; V_I, P_I) = \frac{1}{\sqrt{rA_1}} \left(\text{atan} \left[\sqrt{\frac{rA_1}{D_1 - rA_1(V - B_1)^2}} (V - B_1) \right] - \text{atan} \left[\sqrt{\frac{rA_1}{D_1 - rA_1(V_I - B_1)^2}} (V_I - B_1) \right] \right) \quad [\text{S113}]$$

$$X_2(V; V_I, P_I) = \frac{1}{\sqrt{rA_2}} \left(\text{atan} \left[\sqrt{\frac{rA_2}{D_2 - rA_2(V - B_2)^2}} (V - B_2) \right] - \text{atan} \left[\sqrt{\frac{rA_2}{D_2 - rA_2(V_b - B_2)^2}} (V_b - B_2) \right] \right) + X_1(V_b; V_I, P_I) \quad [\text{S114}]$$

$$X_3(V; V_I, P_I) = \frac{1}{\sqrt{rA_3}} \left(\text{atan} \left[\sqrt{\frac{rA_3}{D_3 - rA_3(V - B_3)^2}} (V - B_3) \right] - \text{atan} \left[\sqrt{\frac{rA_3}{D_3 - rA_3(W_{\text{Na}} - B_3)^2}} (W_{\text{Na}} - B_3) \right] \right) + X_2(W_{\text{Na}}; V_I, P_I) \quad [\text{S115}]$$

Since we now know the solution $x(V; V_I, P_I)$ for arbitrary initial conditions, we can explicitly compute the curves highlighted in the main text. For example, suppose we wish to compute $X(V)$ from Eq. (M62). First we note that $V_1(V)$ is given by solving $P(V; V_1, \sqrt{m}V_1) = 0$, yielding

$$V_1(V) = \sum_i \frac{rA_1B_1 + \sqrt{r^2A_1^2B_1^2 - r(m + rA_1)(A_1B_1^2 - A_i(V - B_i)^2 + C_1 - C_i)}}{rA_1 + m} \Theta_i(V) \quad [\text{S116}]$$

In Eq. (S116), we have assumed that $r < \frac{mV_b^2}{V_{\text{Na}} + bW_{\text{Na}} - V_b(1+b)}$, so that $V_1 \in [0, V_b]$. Then we obtain $X(V)$ by substituting

$$X(V) = x[V; V_1(V), \sqrt{m}V_1(V)] \quad [\text{S117}]$$

More explicitly:

$$X(V \in [0, V_b]) = \frac{1}{\sqrt{rA_1}} \left(\frac{\pi}{2} - \text{atan} \left[\sqrt{\frac{rA_1}{D_1 - rA_1(V_1 - B_1)^2}} (V_1 - B_1) \right] \right) \quad [\text{S118}]$$

$$X(V \in [V_b, W_{\text{Na}}]) = \frac{1}{\sqrt{rA_2}} \left(\frac{\pi}{2} - \text{atan} \left[\sqrt{\frac{rA_2}{D_2 - rA_2(V_b - B_2)^2}} (V_b - B_2) \right] \right) + X_1(V_b; V_1, \sqrt{m}V_1) \quad [\text{S119}]$$

$$X(V \in [W_{\text{Na}}, V_{\text{Na}}]) = \frac{1}{\sqrt{rA_3}} \left(\frac{\pi}{2} - \text{atan} \left[\sqrt{\frac{rA_3}{D_3 - rA_3(W_{\text{Na}} - B_3)^2}} (W_{\text{Na}} - B_3) \right] \right) + X_2(W_{\text{Na}}; V_1, \sqrt{m}V_1) \quad [\text{S120}]$$

141 where the V dependence enters through $D_i[V_1(V)]$ and $V_1(V)$.

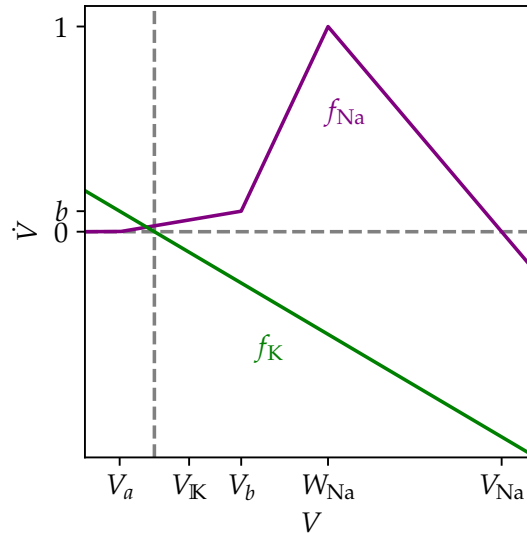


Fig. S7. Piecewise linear ion channels.

7. Preliminaries on the Conley index

A. Homotopy Conley index. Here we provide supplemental background on the Conley index (5, 6) and provide derivations of the associated results used in Methods §B. Let X be a metric space. A flow ϕ on X is a continuous map $\phi : X \times \mathbb{R} \rightarrow X$ obeying the following conditions $\phi(x, 0) = x$ and $\phi(x, a + b) = \phi(\phi(x, a), b)$ for all $x \in X$ and $a, b \in \mathbb{R}$. An invariant set $S \subset X$ is one which obeys $\phi(S, \mathbb{R}) = S$. In other words, it is any union of solution curves of the flow. Given a set $N \subset X$, we define $\text{inv}(N) = \{x \in N : \phi(x, \mathbb{R}) \subset N\}$. A compact set N is known as an isolating set if $\text{inv}(N) \cap \partial N = \emptyset$. We say that an isolating set N is an isolating neighborhood of the invariant set S if $S = \text{inv}(N)$. An invariant set S is an isolated invariant set if it permits an isolating neighborhood. A pair of compact sets (N, L) with $L \subset N$ is known as an index pair if they satisfy the three following conditions:

1. $\text{cl}(N \setminus L)$ is an isolating set
2. L is forward invariant in N . That is $N \cap \phi(L, [0, \infty)) \subset L$.
3. L is an exit set for N . That is for all $x \in N$, if $\phi(x, [0, \infty)) \not\subset N$, then there exists $t > 0$ such that $\phi(x, [0, t)) \subset N$ and $\phi(x, t) \in L$.

We say that (N, L) is an index pair for an isolated invariant set S if $S = \text{inv}(N \setminus L)$. One can show that for every isolating set N , there exists an index pair for $\text{inv}(N)$. Given an index pair, we define the homotopy Conley index as follows

$$h(N, L) = \overline{(N/L, [L])} \quad [\text{S121}]$$

Here, the notation $(N/L, [L])$ denotes the pointed topological space formed by the quotient of N and L , i.e. the space formed by identifying L to a single point. Given a pointed topological space (Y, y) , the notation $\overline{(Y, y)}$ denotes the equivalence class of all topological spaces that are homotopically equivalent to Y with fixed point y . If (N, L) and (N', L') are both index pairs for the isolated invariant set S , then one can show that $h(N, L) = h(N', L')$. Hence, given an isolated invariant set S , it is unambiguous to write $h(S)$ and refer to the Conley index as an intrinsic property of the isolated invariant set.

The Conley index obeys two crucial properties typical of topological indices. First, it obeys an addition formula: If S_1 and S_2 are disjoint isolated invariant sets, then

$$h(S_1 \sqcup S_2) = h(S_1) \vee h(S_2) \quad [\text{S122}]$$

where \sqcup is the disjoint union and \vee is the wedge sum, which glues two pointed spaces together by identifying their distinguished points. Second, $h(S)$ has a continuity property. Suppose ϕ_λ has a continuous parameter $\lambda \in \Lambda$. If N_λ is continuous in λ and N_λ is an isolating neighborhood for all $\lambda \in \Lambda$, then $h(\text{inv}(N_\lambda)) = h(\text{inv}(N_{\lambda'}))$ for all $\lambda, \lambda' \in \Lambda$. Hence, we can deform flows and isolating neighborhoods, and so long as the isolated invariant sets do not intersect the boundaries of the proposed isolating neighborhoods, the index is invariant throughout the deformation.

In practice, the following facts are frequently used. For a hyperbolic fixed point p , $h(p) = \overline{\Sigma^d}$, where Σ^d is the pointed d -sphere and d is the unstable dimension of the fixed point. Also, if an isolating neighborhood N does not contain an isolated invariant set, then $\text{inv}(N) = \emptyset$, and $h(\emptyset) = \overline{0}$, where $\overline{0}$ denotes the space with a single point. This yields a seemingly simple but useful existence theorem: if $h(\text{inv}(N)) \neq \overline{0}$, then N must contain an isolated invariant set. This is useful because computing $h(\text{inv}(N))$ only requires information about ϕ on the boundary of N . Hence, one can choose N wisely to simplify computations of $h(\text{inv}(N))$. Finally, we note that for a hyperbolic fixed point p , the unstable dimension d is also known as the Morse index. For this reason, the Conley index may be thought of as generalization of the Morse index that is defined for any isolated invariant set, not just fixed points.

B. Homological Conley index. Homology theory is a set of algebraic tools for studying homotopy type classes. Given topological spaces $X \subset Y$, their relative homology refers to a sequence

$$H(Y, X) = (H_0(Y, X), H_1(Y, X), \dots) \quad [\text{S123}]$$

where each H_n is an abelian group. For a pointed space (Y, y) , the reduced homology of Y is defined as $H(Y) \equiv H(Y, y)$. There are multiple varieties of homology (i.e. different ways of assigning the sequence of abelian groups to topological spaces) that encode different types of topological information. Alexander-Spanier homology is a standard choice for Conley index theory. (We will simply state the facts that we need without offering a full definition.) All types of homology have the following two properties (among others). First, given two homotopically equivalent pointed topological space Y and Y' , $H(Y) \cong H(Y')$, where \cong denotes isomorphism. Hence, we can unambiguously talk about H as being a map from homotopy equivalence classes to graded abelian groups. Next, there is a useful addition property:

$$H(Y \vee Y') \cong H(Y) \oplus H(Y') \quad [\text{S124}]$$

Finally, if $X \subset Y \subset Z$, then

$$\dots \rightarrow H_n(Y, X) \rightarrow H_n(Z, X) \rightarrow H_n(Z, Y) \rightarrow H_{n-1}(Y, X) \rightarrow \dots \quad [\text{S125}]$$

is an exact sequence. By *exact sequence*, we mean that there exists homomorphisms between subsequent groups in the sequence and the image of one homomorphism is equal to the kernel of the next. Exact sequences are a useful construction for the following reason: if Eq. (S125) contains a subsequence of the form $0 \rightarrow A \rightarrow B \rightarrow 0$, then the exactness property implies $A \cong B$. For our purposes, the only homology groups that we will explicitly need are those of spheres:

$$H_n(\Sigma^d) = \begin{cases} 0 & n \neq d \\ \mathbb{Z} & n = d \end{cases} \quad [\text{S126}]$$

173 and for the single point $H(\bar{0}) = 0$. In the context of Conley index theory, homology theory is used as follows. For any isolated
174 invariant set S , one can always find an index pair (N, L) such that $H(N, L) = H(N/L, [L]) = H(h(S))$. The quantity $H(h(S))$
175 is known as the homological Conley index.

C. Morse decompositions. For $x \in X$, define $\alpha(x) = \bigcap_t \text{cl}(\phi(x, (-\infty, -t)))$ and $\omega(x) = \bigcap_t \text{cl}(\phi(x, (t, \infty)))$. Given an isolated invariant set S , a Morse decomposition of S is a finite list (S_1, S_2, \dots, S_n) of isolated invariant sets with $S_i \subset S$ such that for all $x \in S \setminus \sqcup_i S_i$ there exists $j < k$ such that $\omega(x) \subset S_j$ and $\alpha(x) \subset S_k$. For every Morse decomposition, there exists a sequence of isolating sets (N_0, N_1, \dots, N_n) such that (N_n, N_0) is an index pair for S and (N_i, N_{i-1}) is an index pair for S_i . Such a sequence is known as a Morse filtration. The notion of a Morse filtration is useful in conjunction with Eq. (S125). Given a subset (N_{i-1}, N_i, N_{i+1}) , one then obtains the exact sequence:

$$\cdots \rightarrow H_n(h(S_{i-1})) \rightarrow H_n(N_{i+1}, N_{i-1}) \rightarrow H_n(h(S_i)) \rightarrow H_{n-1}(h(S_{i-1})) \rightarrow \cdots \quad [\text{S127}]$$

176 It turns out that (N_{i+1}, N_{i-1}) is itself an index pair.

177 **D. Stability lemma.** Following Ref. (7), we will use the above structure to prove the following lemma. Suppose N is an isolating
178 set with respect to gradient flow ϕ . Suppose $h(\text{inv}(N)) = \bar{0}$ and N contains exactly two fixed points a and b , and let d_a and d_b
179 denote their unstable dimensions. Then $d_a = d_b \pm 1$ and there exists a heteroclinic orbit from a to b if the $-$ is taken, and from
180 b to a if the $+$ is taken.

To prove this, notice that $h(a) \vee h(b) = \overline{\Sigma^{d_a} \vee \Sigma^{d_b}} \neq \bar{0}$. Hence, there must be additional isolated invariant sets in N . Since we are considering gradient flow, the only possible additional isolated invariant set is a heteroclinic orbit flowing from a to b or from b to a . Without loss of generality, we assume the flow runs from a to b . Then (b, a) constitutes a Morse decomposition, so there exists a Morse filtration (N_0, N_1, N) . This Morse filtration gives rise to the exact sequence

$$\cdots \rightarrow H_n(\Sigma^{d_b}) \rightarrow H_n(\bar{0}) \rightarrow H_n(\Sigma^{d_a}) \rightarrow H_{n-1}(\Sigma^{d_b}) \rightarrow \cdots \quad [\text{S128}]$$

But noting that $H_n(\bar{0}) = 0$ and using Eq. (S126), we obtain the short exact sequence:

$$0 \rightarrow \mathbb{Z} \rightarrow H_{d_a-1}(\Sigma^{d_b}) \rightarrow 0 \quad [\text{S129}]$$

181 The short exact sequence in Eq. (S129) implies that $\mathbb{Z} \cong H_{d_a-1}(\Sigma^{d_b})$, which implies through Eq. (S126) that $d_a = d_b + 1$, as
182 desired.

Movie S1. Experimental observation of spiking at a bioelectric interface:

Two tissues of human embryonic kidney (HEK293) cells were genetically modified to express either sodium ($\text{Na}_v1.5$) or potassium ($\text{K}_{ir}2.1$) channels. Neither tissue alone is able to spike. However, upon stimulation by a laser, an action potential is observed to propagate along their interface, as revealed by a voltage sensitive red dye. Adapted from Ref. (8).

Movie S2. 2D nonlinear waveguides built from excitable interfaces:

A network of excitable interfaces forms a two-dimensional nonlinear waveguide capable of performing computations. Simulations of the binary half adder in Fig. 5c-d are shown. See SI §5 for details of the numerics.

References

1. J Murray, *Mathematical Biology: I. An Introduction*, Interdisciplinary Applied Mathematics. (Springer New York), (2013).
2. KHWJ ten Tusscher, D Noble, PJ Noble, AV Panfilov, A model for human ventricular tissue. *Am. J. Physiol. Circ. Physiol.* **286**, H1573–H1589 (2004) PMID: 14656705.
3. RJ Field, E Koros, RM Noyes, Oscillations in chemical systems. II. Thorough analysis of temporal oscillation in the bromate-cerium-malonic acid system. *J. Am. Chem. Soc.* **94**, 8649–8664 (1972).
4. JJ Tyson, *The Belousov-Zhabotinskii reaction*, Lecture notes in biomathematics. (Springer-Verlag, Berlin; New York), (1976).
5. C Conley, C Sciences, *Isolated Invariant Sets and the Morse Index*, Conference Board of the Mathematical Sciences Series No. 38. (American Mathematical Society) No. no. 38, (1978).
6. K Mischaikow, M Mrozek, Conley index in *Handbook of Dynamical Systems*, ed. B Fiedler. (Elsevier Science) Vol. 2, pp. 393–460 (2002).
7. CC Conley, JA Smoller, *Algebraic and Topological Invariants for Reaction-Diffusion Equations*, ed. JM Ball. (Springer Netherlands, Dordrecht), pp. 3–24 (1983).
8. H Ori, et al., Observation of topological action potentials in engineered tissues. *Nat. Phys.* **19**, 290–296 (2023).